Master´s Thesis

Chromium-doped copper vanadate films ($Cr:Cu_3V_2O_8$) as photoanodes for water splitting

Drialys Cárdenas Morcoso

Castellón de la Plana, July 2016

Chromium-doped copper vanadate films ($Cr:Cu_3V_2O_8$) as photoanodes for water splitting

Thesis presented in option to the

Master´s Degree in Applied Physics

Author: Drialys Cárdenas Morcoso

Director: Dr. Sixto Gimenez

Castellón de la Plana, July 2016

To my grandma Emilia

Acknowledgments

I would like to thank the financial support from the University Jaume I through the project P1·1B2011-50 and from the Generalitat Valenciana, through the Santiago Grisolia Program, grant 2015-031, for which it has been possible to carry out this investigation.

To the Serveis Centrals at UJI (SCIC), were structural and morphological characterizations were done.

Specially, thanks to Dr. Sixto Gimenez for allow me to joining in his research group, for all that I learned in this time and for his constant concern with my job and results.

Also thanks to Isaac Herraiz-Cardona for all their help inside the lab, in the discussions of the results and, in general, all the knowledge shared in this time.

In general, to all the people of the GDFO and their leader Prof. Juan Bisquert, which have welcomed me, especially to Marta, Lucía and Nuria, for becoming such good friends in a country where I had no one.

And of course to my family and friends in Cuba, who have supported and encouraged me all this time from the distance.

Abstract

Solar hydrogen obtained from photoelectrochemical water splitting offers a versatile approach towards the substitution of fossil fuels by decentralized and sustainable resources, like water and sun. In the present study, chromium-doped copper vanadate ($Cr:Cu_3V_2O_8$) was investigated as a promising photoanode candidate for photoelectrochemical water splitting. This material was synthesized through a simple aqueous precipitation reaction, which easily allows compositional modifications. The optimal conditions for a reproducible synthesis, film thickness and dopant content were stablished. The effect of extrinsic doping with substitutional atoms like Chromium on the optical and photoelectrochemical properties of this material was studied. Furthermore, key electronic properties for the evaluation of this material as photoanode such as band gap and valence band position, flat band potential and donor density were determined. A three-fold enhancement in the photocurrent obtained was reached for 800 nm thin films with a 0.75 at. % content of Chromium (with respect the Copper content). It was found that the main limiting factor for performance of this material is related to the high bulk recombination, which is partially ameliorated by 0.75 at. % Chromium doping, with a five-fold enhancement of the charge separation efficiency at 1.23 V vs RHE.

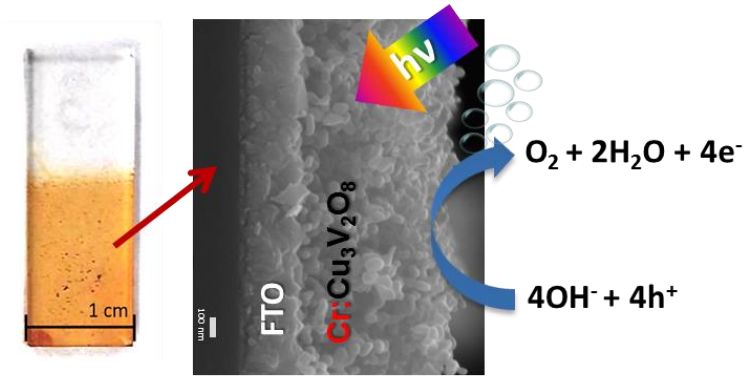

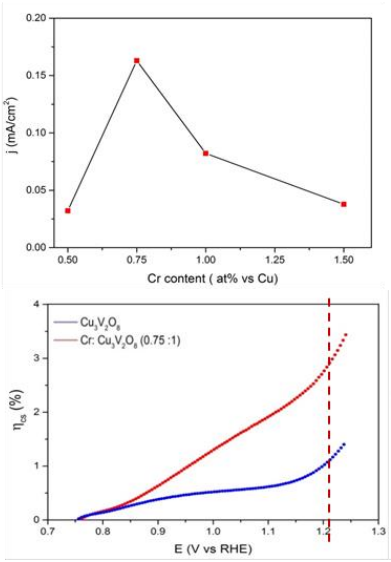

CONTENT

Introduction

The sun feeds the planet with an enormous amount of power, ~120 000 TW, which considerably exceeds the projected global energy demand for the next decades (~30 TW by 2050) in a moderate scenario.[1] Therefore, the conversion of sunlight into a profitable form of energy is almost mandatory to meet the needs of a growing world population with increasing living standards. On the other hand, not only conversion but large-scale use of solar energy requires both an efficient energy storage solution and an environmental friendly harnessing of the sunlight into solar fuels.

It has been proved that a practical way to store such large amounts of energy is in the form of a chemical energy carrier, i.e., a fuel. In particular, hydrogen is one of the prime candidates as a future energy carrier offering great advantages because it has a high energy density and its use as fuel produces almost no pollution. It can be obtained from a very abundant resource as water, and upon combustion in a fuel cell it returns to its original form, water. Significantly higher emission of pollutants is related to fossil energy systems (e.g. CO, CO_2, C_nH_m, SO_x, NO_x, ashes) highlighting the cleaner energy conversion processes stemming from renewable hydrogen energy system.[2]

The future prospect of a so-called *Hydrogen Economy* to replace our current energy economies has attracted much interest, and many research efforts are currently underway to develop new technologies for the production, storage, utilization, and transport of hydrogen.[3]

Concerning to the production, one of the most attractive ways to obtain hydrogen as solar fuel is through water splitting, which can be achieved by three representative methods: electrolysis powered by photovoltaics, particulate photocatalysis and photoelectrochemical (PEC) water splitting. While photovoltaic electrolysis is a high efficiency, yet high-cost method, particulate photocatalysis is a low-cost system but it requires the separation of the explosive hydrogen and oxygen gas mixture generated, which consume additional energy, hence, reducing the overall water splitting efficiency. Meanwhile, PEC water splitting possesses a potential high efficiency, up to >30 % in principle[4], and is a relatively low-cost method. In this process, a photo-active semiconductor is immersed in an aqueous electrolyte and the photo-generated charge carriers are directly used to reduce and oxidize water. Since the half reactions for H_2 and O_2 evolution can be spatially separated, PEC water splitting does not require additional gas separation process and allows each to be optimized independently.

In the present year (2016), 96% of global hydrogen production is from fossil fuels (48% from natural gas, 30% from oil, and 18% from coal), while water electrolysis accounts only for 4%.[5] Since the pioneering study of Fujishima and Honda[6], intensive research efforts have been carried out to find efficient, stable and low-cost materials that can absorb a significant fraction of the solar spectrum to split water. In particular, the efficient operation of the water oxidation reaction, which takes place in the

(photo)anode, is a fundamental requirement to obtain PEC solar fuels at high solar-to-hydrogen efficiency (STH).

$Cu_3V_2O_8$ is an *n*-type semiconductor composed only of first-row transition metals with adequate band gap and band position to act as photoanode in a PEC water splitting solar cell.

*The **Objective** of this Master´s Thesis is to investigate the effect of the film thickness and the Cr incorporation to the $Cu_3V_2O_8$ structure, on the structural, optical, electrical and photoelectrochemical features of this promising material.* This study aims:

1. To set the synthesis parameters to optimize the photoanode preparation regarding to dopant content and thickness of the final electrode.

2. To study the three fundamental processes in PEC (charge carrier generation, charge transport to the solid-liquid interface and interfacial charge transfer), based on detailed description of optical and electrical properties of both the bare and the doped $Cu_3V_2O_8$ films in order to achieve a better understanding of this material and to propose new routes to improve their PEC performance.

In Chapter 1, a detailed description of PEC solar cell performance is presented, as well as the recent advances related, in particular, with semiconductor materials employed as photoanodes, highlighting the current challenges. Also, the main properties of $Cu_2V_3O_8$ oxide are described as a promising photoanode material for PEC water splitting and our proposals to improve its behavior.

In Chapter 2, the synthesis methods and the specific parameters in the electrode preparation with particular emphasis on controlling the film thickness are detailed. All the characterization techniques employed to investigate the effect of doping on this material are also described.

Finally, in Chapter 3, the results of a detailed optoelectronic and photoelectrochemical characterization, aiming at quantitatively addressing the contribution of the charge carrier generation, charge transport to the solid-liquid interface and interfacial charge transfer to the obtained photocurrent density are presented.

Chapter 1: State of the art on PEC solar cells

1.1 Solar PEC water splitting cells

Photoelectrochemical (PEC) water splitting, demonstrated first by Fujishima and Honda,[6] offers an attractive technology for the conversion and storage of solar energy as chemical energy in the form of the molecular bonds of the H_2 molecule. As shown in Figure 1.1a, in this process, the water molecule is decomposed into H_2 and O_2 under solar illumination, with a Gibbs energy of 237 kJ mol^{-1}, through the reactions (in alkaline media):

$$4OH^-(aq) \rightarrow O_2(g) + 2H_2O(l) + 4e^-,\ E_{red}^{\circ} = 1.23V\ (vs.RHE) \quad (1.1)$$

$$4H_2O(l) + 4e^-(aq) \rightarrow 2H_2(g) + 4OH^-(aq),\ E_{red}^{\circ} = 0V\ (vs.RHE) \quad (1.2)$$

And in acid media:

$$2H_2O(l) \rightarrow O_2(g) + 4H^+(aq) + 4e^-,\ E_{red}^{\circ} = 1.23V\ (vs.RHE) \quad (1.3)$$

$$4H^+ + 4e^-(aq) \rightarrow 2H_2(g),\ E_{red}^{\circ} = 0V\ (vs.RHE) \quad (1.4)$$

When the semiconductor is illuminated with photons that have an energy equal to or larger than the bandgap (E_g), electrons are excited from the valence band (VB) into the conduction band (CB) generating an electron-hole pair (Figure 1.1b). In an *n*-type semiconductor (photoanode), the holes in the VB migrate to the surface upon illumination, where they react with the aqueous redox electrolyte to oxidize water to form oxygen gas, the O_2 evolution reaction, OER (eq. 1.1;1.3). The electrons in the CB travel to the back contact and are transported to the counter electrode, where they reduce water to produce hydrogen gas (H_2) (eq. 1.2;1.4) [4]. In analogy, a photocathode and a light-inactive anode could be also used, or both light active electrodes.

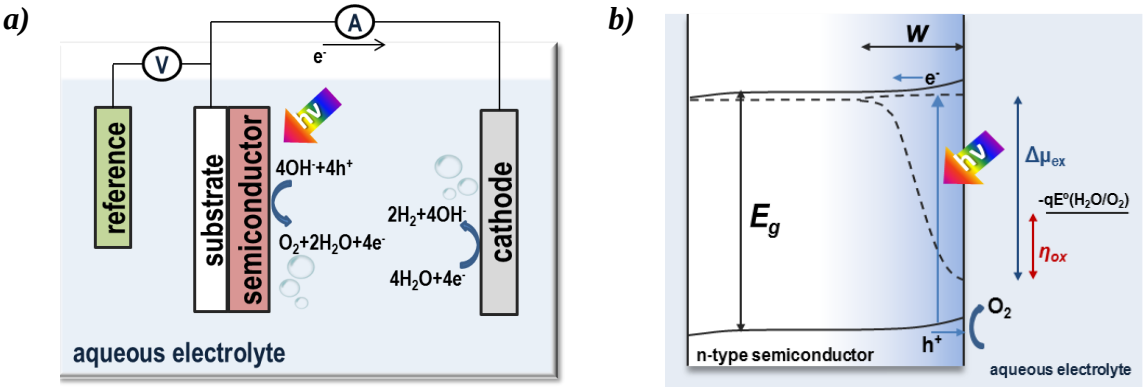

Figure 1.1 a) Schematic representation of PEC water splitting cell and b) electron energy scheme of a *n*-type semiconductor in alkaline aqueous electrolyte.

In this process, the OER is thermodynamically and kinetically more demanding, since four holes per molecule of produced oxygen are required.[4,7] The strong oxidizing conditions needed for this reaction severely limit the choice of adequate materials for viable operation. Consequently, the development of efficient and stable oxygen evolving photoanodes is one of the key challenges to success of this technology.[7]

From the picture above, it could be seen that suitable photo-electrode materials for efficient solar hydrogen generation have to fulfill the following requirements:

1) ***Strong (visible) light absorption:*** The spectral region in which the semiconductor material absorbs light is determined by the E_g. Water splitting is not a spontaneous process but requires an energy supply equivalent to 1.23 eV. However, an extra energy input is needed due to the thermodynamic losses (~230.4 eV) and overpotential required due to kinetics mechanisms (~0.3-0.4 eV).[3] On the other hand, the maximum value of the bandgap is determined by the solar spectrum. As it is show in Figure 1.2, below 400 nm (3.1 eV) the sunlight intensity falls abruptly, so absorption below this wavelength would use only a very small portion of the solar spectrum. Thus, the optimum semiconductor E_g must be between 1.9 eV and 3.1 eV (650-400 nm on the visible range of the solar spectrum). The theoretical maximum efficiency for an ideal material with E_g = 2.03 eV is 16.8%.[8] Higher efficiencies can be obtained by using a multiple-bandgap system.

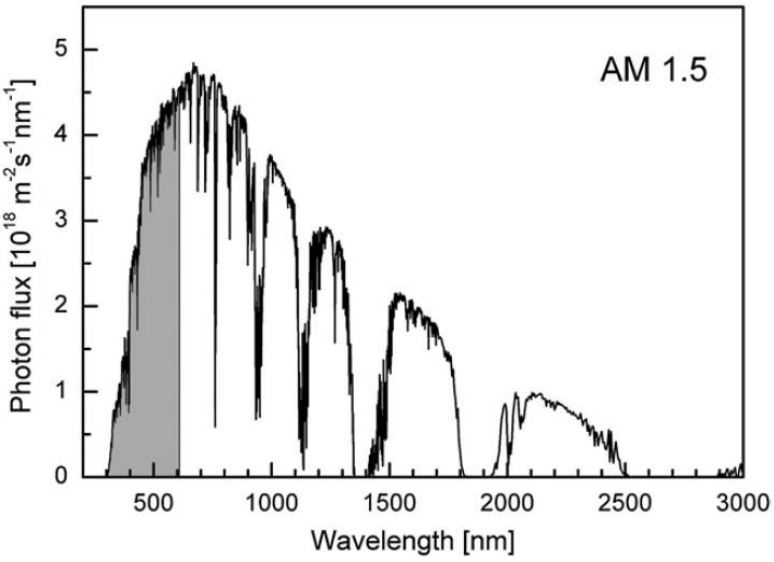

Figure 1.2 Intensity of sunlight *vs.* wavelength for AM1.5 conditions. The grey area represents the part of the spectrum that can be absorbed by a hypothetically ideal bandgap of 2.03 eV.[3]

2) ***High chemical stability in dark and under illumination:*** For practical purposes, the employed semiconductor materials should be stable in aqueous medium for a long time, under both light and dark conditions. Usually, metal oxide semiconductors with larger E_g are more stable against photo-corrosion. In some cases, the stability appears to depend on the presence of dopants, pH and oxygen stoichiometry.

3) ***Suitable band edge positions to enable reduction/oxidation of water*:** As shown in Figure 1.1b and eq. (1.1-4) to carry out the water splitting process (both OER and HER) the VB of the semiconductor must be located below the oxidation potential of water, while CB should be above hydrogen reduction potential. Most semiconductor oxides are capable of oxidizing water but not to reduce it, whereby they are usually employed in tandem configuration.

4) ***Efficient charge transport in the semiconductor:*** Charge transport (conductivity) from bulk to contact should be efficient. In materials with good conductivity, the electron-hole recombination in the bulk will be lower and thus the water splitting efficiency will be higher. This requirement is the main cause of the low conversion efficiency in most metal semiconductor oxides.

5) ***Low overpotentials for the reduction/oxidation reactions:*** Charge transfer at the semiconductor/electrolyte interface must be fast to avoid charge accumulation on the surface and thus increase the electron-hole recombination in this region. In order to reduce efficiency losses due to charge transfer on the surface, it is common the use of catalysts.

6) ***Low cost:*** The materials employed for PEC water splitting must be, if they are not naturally available, at least obtained through low cost and environmental friendly synthetic preparation technics, starting from abundant and non-toxic materials, with low temperatures and short time synthesis, in order to guarantee the competition with other hydrogen generation technologies.

Despite extensive research efforts, mainly in the 1970´s and early 1980´s, no photo-active material that fulfills all these requirements has been found yet. There are two main ways to deal with this challenge: to discover new materials having unique properties for solar water splitting purposes or to use additional technological means, such as doping with other elements, constructing appropriate heterojunctions, introducing suitable co-catalysts, etc., to improve the existing materials.

1.2 Metal oxide semiconductors for PEC water splitting. Recent advances and challenges.

As discussed above, to find semiconductor materials that fulfill all the requirements described is still a challenge. Particularly, for photoanodes, one of the most challenging requirements is related to the stability to photo-corrosion. In principle, in metal oxide photoanodes, the photo-generated holes are able to oxidize the semiconductor. However, if the kinetics of charge transfer across the interface (oxidation of water) are faster than the anodic decomposition reaction, photo-corrosion is avoided.[3] In terms of band positions, when the standard electrode potential for the anodic dissolution of the electrode material is more positive than the VB edge, the electrode should be anodically stable. This means that an *n*-type semiconductor may be anodically stable even if the

anodic dissolution potential is more negative than the VB edge when a redox potential for the reactant in an electrolyte is lower than that for the anodic dissolution potential.

Figure 1.3 shows the band-edge position of some semiconductor materials that have been studied for PEC water splitting applications. As can be seen, in particular, metal oxides or oxo-metalates based on abundant materials, such as TiO_2,[9,10] Fe_2O_3,[11] and WO_3[12] have an adequate band position to carry out the oxidation reaction, so they have been predominantly tested as photoanode materials, satisfying both stability and cost requirements.

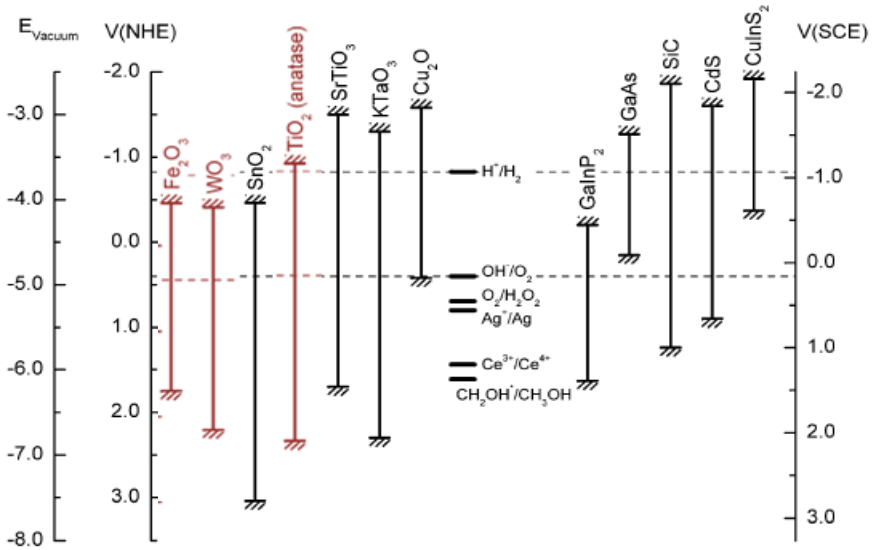

Figure 1.3 Energy band positions for various semiconductors at pH 14 [3]

Nevertheless, the low performance of these photoanodes attributed to poor electronic properties (eg. Fe_2O_3) and/or large bandgaps (TiO_2, WO_3) hinder their large-scale usage in PEC systems. On the other hand, the dependence of electronic and optical properties of semiconductors with their size and morphology have been proved, therefore this constitutes also an important parameter to take into account during the preparation of these materials. In order to overcome these problems, different strategies have been accomplished, involving combinatorial synthesis,[13] tuning the band structure of semiconductor materials by doping with different elements,[14-15] surface state passivation,[16-17] surface activation with OER catalysts,[18-19] and nanostructuring strategies.[20-23]

In general, the advent of nanotechnology has produced a dramatic increase in the photocurrent delivered by these oxides through careful nanoestructuring and doping strategies. These approaches enhance light harvesting by increasing the probability of a photogenerated hole to reach the semiconductor/electrolyte interface and improve the transport of the majority carriers (electrons) to the substrate.

Metal vanadates, mainly $BiVO_4$, are at the forefront of the research for PEC water splitting photoanodes.[14, 18, 20] One of the main limitations of $BiVO_4$ has been attributed to the slow transfer of photogenerated holes from the $BiVO_4$ to the electrolyte, as shown

by various studies involving the use of holes scavengers. The second limitation of $BiVO_4$ is its poor charge transport properties, which has been significantly improved by doping with W and Mo.[24] At present, a record photocurrent density of 6.7 $mA \cdot cm^{-2}$ at 1.23 V vs RHE close to the theoretical maximum photocurrent density of 7.5 mA/cm^2 was obtained for $BiVO_4$, achieved by employing a $BiVO_4/WO_3$ guest-host nanostructure modified with a Co-Pi oxygen evolution catalyst.[25]

More recent developments include the identification of a divalent Mn vanadate, β-$Mn_2V_2O_7$, with a 1.8 eV direct band gap and excellent band alignment to the OER equilibrium potential.[26] Triclinic NiV_2O_6 films, fabricated by a vacuum deposition technique, have been recently tested for the first time as photoanodes for water oxidation. [27] Although the observed photocurrent is relatively low (ca. 0.25 $mA \cdot cm^{-2}$ at 1.23 V vs RHE) according to the band gap (~2.4 eV) both the wide availability of the semiconductor components (Ni and V) and its stability in alkaline conditions postulate this material as a promising anode for PEC systems.

A set of divalent Cu vanadates have also been reported as photoanodes. The CuO–V_2O_5 system is rapidly emerging as the most prominent composition system for OER photoelectrocatalysts. It has been reported OER photoelectrocatalysis with $Cu_{11}V_6O_{26}$, γ-$Cu_3V_2O_8$, α-$Cu_2V_2O_7$, and β-$Cu_2V_2O_7$ photoanodes in pH 7, pH 9.2 and pH 13 electrolytes.[28-30] The experimental and computational assessments of the optical properties of these phases indicate that they are all indirect E_g semiconductors with E_g near or below 2 eV.[26] It has been found that the photoelectrochemical activity is particularly promising in borate-buffered pH 9.2 electrolytes.

1.3 $Cu_3V_2O_8$ as a promising photoanode for PEC water splitting.

$Cu_3V_2O_8$ is an *n*-type semiconductor composed only of first-row transition metals. Although this material has been previously examined for different applications as Li-ion batteries and degradation of organic pollutants,[31-32] both, its bandgap near 2.0 eV and the adequate position of the valence band maximum ($2.5 \leq E_{VB} \leq 2.7$ V) [30] make this material suitable for water photo-oxidation.

Regarding the crystalline structure, the $Cu_3V_2O_8$ has an interesting crystal structure of porous frame-work that consists of Cu-O octahedra and V-O tetrahedra. The $Cu_3V_2O_8$, also known as orthovanadate $Cu_3(VO_4)_2$, presents two polymorphic transitions at 460 and 540°C which are rapid and reversible, but the structures of the high-temperature phases are unknown. It has been reported that for T < 460 ºC, $Cu_3V_2O_8$ crystallizes into triclinic *P*-1; the β-$Cu_3V_2O_8$ monoclinic *P*21/*c* was observed for 460 ºC < T < 540 ºC meanwhile the γ-$Cu_3V_2O_8$ orthorhombic *Cmca* was reported for 540 < T < 780 ºC.[33] This material also presents, above 3 GPa at 900°C, a high pressure modification $Cu_3V_2O_8$-II, which may also be obtained by thermal decomposition above 400°C of the mineral $Cu_3V_2O_8 \cdot 3H_2O$ (volborthite), that is actually a basic pyrovanadate whose exact formula is $Cu_3V_2O_7 \cdot (OH)_2 \cdot 2H_2O$. In both phases, Cu^{2+} ions are located at octahedral sites. The monoclinic variety of $Cu_3V_2O_8$, space group *P*21/*c*, type

$Mg_3(VO_4)_2$ described by as β-$Cu_3V_2O_8$ (Figure 1.4), stable at room temperature, is actually the high pressure modification $Cu_3V_2O_8$-II.[34]

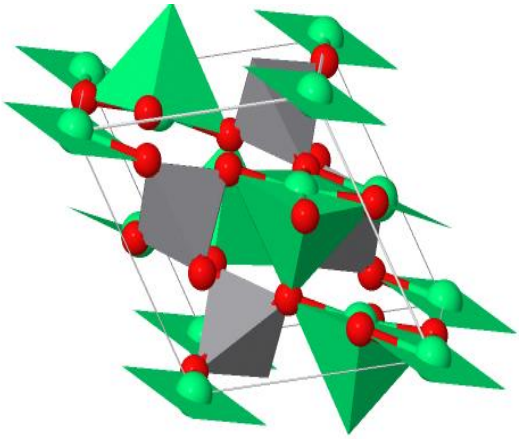

Figure 1.4 Crystalline structure of β-$Cu_3V_2O_8$ monoclinic P21/c in which can be seen the Cu-O octahedra (green) and V-O tetrahedra (grey).

Different synthesis methods have been reported in the preparation of $Cu_3V_2O_8$ nanoparticles mainly for batteries applications. In most of the studies, it is reported the synthesis of this material in nanoparticle forms, for example, the $Cu_3V_2O_8$ hollow nano-spheres synthesis via a liquid precipitation method with colloidal carbon spheres as template,[31] while pure nanoparticles were prepared via ex-situ precipitation approach in presence of Schiff-base ligand as a new capping agent.[35] Shape-controlled $Cu_3V_2O_7(OH)_2 \cdot 2H_2O$ nanoparticles were synthesized through a simple and facile solution route without any surfactants or template by Zhang *et al.* [36], through which simply controlling the reaction conditions,$Cu_3V_2O_7(OH)_2 \cdot 2H_2O$ nanowires, nanoflakes, and nanoparticles can be selectively prepared. As discussed above, the final $Cu_3V_2O_8$ oxide can be obtained by a low temperature and short time annealing. Regarding thin films preparation, Dai *et al.* (2011) reported the synthesis of $Cu_3V_2O_8$ by solid state reaction techniques, which require long times and high temperature.[32]

The electronic properties reported for $Cu_3V_2O_8$, joined to the fact that thin films of this material can be obtained thought a very simple and low cost synthesis by precipitation reaction, make of this semiconductor an interesting choice for its investigation as promising photoanode for a PEC solar cell for water splitting.

To the best of our knowledge, there is only one recent study reporting the PEC performance of $Cu_3V_2O_8$ photoanodes. Seabold and Neale (2015) obtained a photocurrent density of ca. 5 $\mu A \cdot cm^{-2}$ at 1 V vs RHE in 0.1 M potassium borate buffer at pH 9.2 for bare $Cu_3V_2O_8$ samples synthesized from the precipitation of nanoparticles of a simple hydroxide precursor.[30] Most recently, two different copper-based metal vanadates, i.e. CuV_2O_6 and $Cu_2V_2O_7$, were also tested as photoanodes for water splitting achieving photocurrent densities about 25 and 35 $\mu A \cdot cm^{-2}$, respectively, at 1.23V vs RHE in 0.1 M sodium borate buffer solution.[37] In both studies, it was highlighted that

the dominant limitation of Cu-based vanadate materials PEC performance is related to the low charge separation efficiency.

Once this promising oxide has been identified, the next challenges are both to synthetize it in a controlled and reproducible fashion that yield optimized electrodes and to explore adequate strategies in order to confront the identified deficiencies in the material.

As mentioned above, doping constitutes an effective way to tailor the electronic and optical properties of metal oxide semiconductors. In particular, photoanodes doped with cations such as Si, Ti, Pt, Cr, Mo and Al showed enhanced photocurrent density.[4] In $Cu_3V_2O_8$ photoanodes it was found that doping with 0.75 at. % Mo yielded an improvement of 40% in photocurrent, as a consequence of the increase in the electron diffusion length.[30]

With the aim to improve the photoelectrochemical behavior of this promising material, in this study, doping this oxide with Chromium (Cr) is proposed, in order to obtain Cr:$Cu_3V_2O_8$ thin films as potential photoanode for water splitting. Cr was selected based on having an atomic radii of 0.74 Å, close to that of Cu^{2+} (0.73 Å), making feasible the exchange of both atoms in the CuO_6 octahedra of its crystalline structure, enhancing the *n*-type doping of the semiconductor oxide extrinsically. The effect of dopant incorporation in both the structure and morphology and performance of the material as photoanode for water splitting will be evaluated through optical, structural and electrochemical techniques, allowing also set the synthesis parameters for optimized conditions for thickness and dopant concentration of the final electrode.

Chapter 2: Experimental methods

In this chapter, a detailed description of the synthesis method used for the preparation and doping of $Cu_3V_2O_8$ films as well as the experimental techniques for structural, optical and photoelectrochemical analysis of the obtained oxide are described.

2.1 $Cu_3V_2O_8$ and Cr:$Cu_3V_2O_8$ preparation procedures.

Preparation of $Cu_3V_2O_8$ and Cr:$Cu_3V_2O_8$ films started from the synthesis of a precursor composed of a suspension of nanoparticles of $Cu_3V_2O_7(OH)_2{\cdot}2H_2O$, obtained by a simple precipitation reaction method, following the procedure described by *Seabold, 2015* [30], introducing slight modifications in dopant incorporation and precursor deposition. A detailed description of the procedure is presented below.

2.1.1 Synthesis of $Cu_3V_2O_7(OH)_2{\cdot}2H_2O$ precursor

Table 2.1 shows the employed reagents during the synthesis of the precursor.

Table 2.1 List of reagent employed in the precursor synthesis.

Reagent	Quality	Brand
NH_4VO_3	ASC reagent, ≥99.0%	Sigma-Aldrich
$Cu(CH_3COO)_2{\cdot}H_2O$	puriss. p.a. ≥99.0%	Sigma-Aldrich
$CrCl_3{\cdot}6H_2O$	purum p.a. ≥98%).	Sigma-Aldrich
Triton X-100		

First, two 20 mL aqueous solutions of 4.3 mmol of NH_4VO_3 ($NH_4VO_3 + H_2O \rightarrow V_2O_7^{4-} + 2NH_4^+ + 2H^+$) and 6.0 mmol of $Cu(CH_3COO)_2{\cdot}H_2O$ were simultaneously prepared by dissolving the corresponding amounts of each reagent in Milli-Q water and heated to 80 ºC for 5 min with magnetic stirring. The solutions were cooled until room temperature and rapidly mixed in a centrifuge tube, following by strong shaking for 10 min to obtain a light green/yellow suspension of $Cu_3V_2O_7(OH)_2{\cdot}2H_2O$ nanoparticles. The precursor was recovered by successive centrifugation at 4700 rpm for 6 min and washing with absolute ethanol and finally re-suspended in 20 mL of ethanol. The synthesis procedure is summarized in Figure 2.1

From this solution, a fraction was taken and diluted to obtain a 0.22 M copper content solution. Also, a drop of Triton X-100 was added in order to enhance the homogeneity of the deposition.

In order to evaluate the behavior of the photoanode with different dopant concentration and provide an optimum Cr:Cu ratio, Cr:$Cu_3V_2O_7(OH)_2{\cdot}2H_2O$

nanoparticles were prepared by adding the required amount of 0.22 M $CrCl_3 \cdot 6H_2O$ (p.a. ≥ 98%) solution into 10.0 mL of $Cu_3V_2O_7(OH)_2 \cdot 2H_2O$ suspension in order to obtain the desired Cr:Cu ratio (e.g. 75 µL of $CrCl_3 \cdot 6H_2O$ for 0.75 at. % of Cr content).

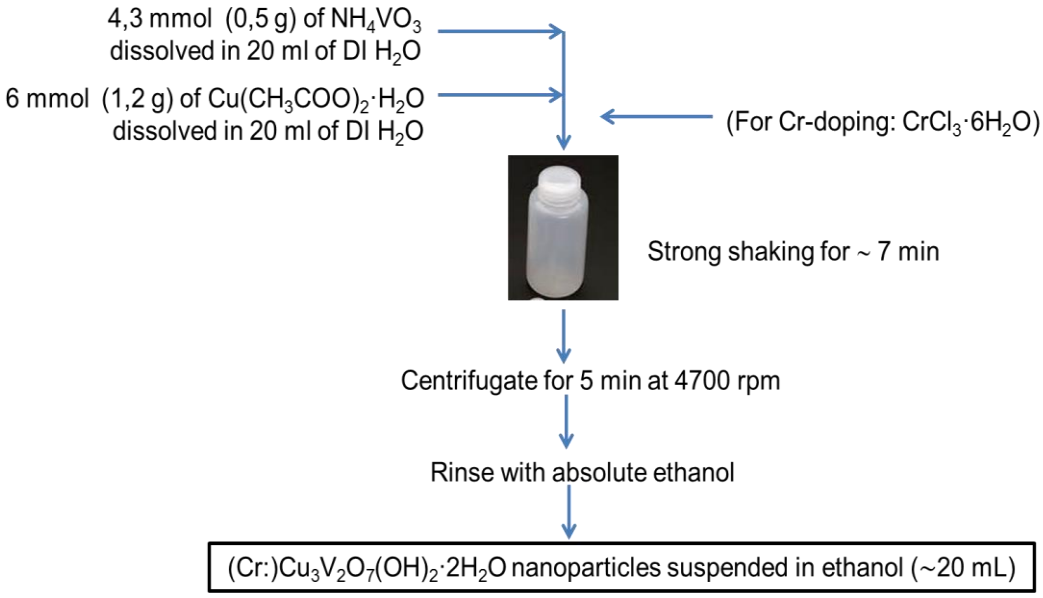

Figure 2.1 Flux diagram of (Cr:)$Cu_3V_2O_7(OH)_2 \cdot 2H_2O$ nanoparticles precursor synthesis.

2.1.2 $Cu_3V_2O_8$ and Cr:$Cu_3V_2O_8$ thin films preparation

Figure 2.2a summarizes the final electrode preparation. Films of different thickness were prepared through the deposition of different number of layers of the $Cu_3V_2O_7(OH)_2 \cdot 2H_2O$ precursor on FTO (fluorine-doped tin oxide) substrate by spin coating. Spin coating was carried out at 3000 rpm for 30 s, using 40 µL of precursor for each deposited layer. These films were dried on a hot plate preheated to 300 °C for 2 min.

Before the precursor deposition, the FTO coated glass electrodes of 3.0 x 1.0 cm^2 area were washed by successive ultra-sonication for 15 min in soap (Hellmanex), Milli-Q water, ethanol, acetone and isopropanol and dried with compressed air. Before the deposition of the nanoparticles, the FTO substrates were treated in a UV−O_3 chamber for 15 min.

To obtain the final oxides, the deposited films were annealed at 425°C for 1 h, preceded by a 2 h ramp up to obtain dark orange oxide films (Figure 2.2b).

a)

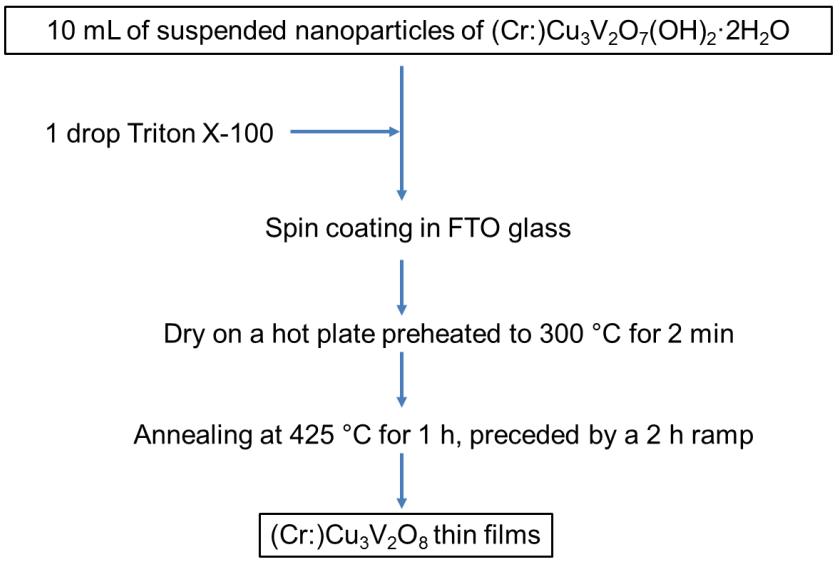

b)

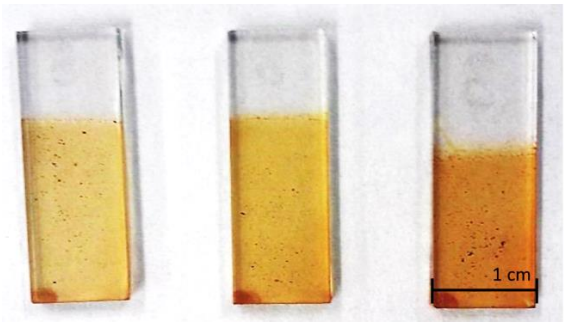

Figure 2.2 ***a)*** Flux diagram of semiconductor films preparation; ***b)*** Photograph of the fabricated photoanode.

2.2 Structural and optical characterization

Crystal structure of both the precursor and oxide films was investigated by X-ray diffraction (XRD). The data were obtained employing Cu K_α radiation at room temperature, scanning the samples from 10º to 70º (2θ) with a step of 0.05º. The recovered patterns were compared with the ISCD data base patterns.

The morphology and thickness were determined by scanning electron microscopy (SEM) using a JEOL JEM-3100F field emission scanning electron microscope.

UV-vis absorption spectra of the oxide films were recovered with a Cary 300 UV−Vis Varian spectrophotometer, between 300 and 800 nm. The absorbance (A) was estimated from transmittance (T) and diffuse reflectance (R) measurements as:

$$A = -\log(T + R). \tag{2.1}$$

From the absorption spectra, the optical bandgap of the semiconductor could be estimated by the Tauc plot as:

$$(h\upsilon\alpha)^{1/n} = A(h\upsilon - E_g) \quad (2.2)$$

were α is the absorption coefficient, $h\upsilon$ the incident light energy and $1/n$ denotes the nature of the transition is represented, which in this case was taken as indirect ($1/n$ = 1/2) based in previous reports on literature for similar vanadates.[28-30]

2.3 Photoelectrochemical characterization

Photoelectrochemical (PEC) measurements were performed using a PGSTAT30 potentiostat from AutoLab in a three-electrode configuration, with a Pt wire as counter electrode and Ag/AgCl, KCl (saturated) as reference electrode in a buffer of 0.1 M H_3BO_3 (≥99.8%, Riedel-deHäen) adjusted to pH 9.2 using KOH. In some cases, a fraction of 0.1 M Na_2SO_3 (≥98%, Sigma-Aldrich) was added to the borate buffer as sacrificial hole scavenger to suppress undesirable surface recombination reactions[38] and increase the hole transfer kinetics at the semiconductor/liquid interface. Photocurrent density (j) measurements were performed through cyclic voltammetry with scan rate of 50 mV s^{-1} and were recorded under AM1.5 100 mW/cm^2 using a Xe lamp previously calibrated with an NREL-calibrated Si solar cell. The working electrode area was 1 cm^2. In all cases, reported potential (E) was referred to the reversible hydrogen electrode (RHE) through the Nernst equation:

$$E_{RHE} = E_{Ag/AgCl} + 0.059\ V\ \times pH \quad (2.4)$$

The same experimental setup was employed for chronoamperometric measurements, which were performed at 1.23 V vs RHE for 1h.

While solar-to-hydrogen efficiency remains the single most important figure of merit to measure the performance of a PEC material/device, other techniques can be used to provide essential information of how the material/device works. One such diagnostic technique is the Incident Photon to Current Conversion Efficiency (IPCE), which may also be refered to as the external quantum efficiency (EQE). The IPCE was measured by employing a 300 W Xe lamp coupled to a monochromator. The photoelectrode was polarized at the desired voltage using and the photocurrent was measured using an optical power meter 70 310 from Oriel Instruments. A Si photodiode was used to measure the light intensity to calibrate the system. IPCE was calculated with the expression:

$$IPCE\ \% = \frac{I_{ph}(A)}{P_\lambda(W)} \times \frac{1239.8\ (Vm)}{\lambda\ (nm)} \times 100 \quad (2.5)$$

where I_{ph} is the photocurrent, the value 1239.8 corresponds to the product hc (Plank´s constant and speed of light respectively), P_λ is the power of light at a particular wavelength, and λ is the wavelength of irradiation.

The maximum obtainable photocurrent under AM1.5 irradiation was estimated by eq. (2.6):

$$j_{AM\ 1.5} = \int (IPCE_\lambda \times \Phi_\lambda \times q) d\lambda \quad (2.6)$$

where $j_{AM\ 1.5}$ is the total photocurrent density under solar irradiation (mA/cm^2), Φ_λ is the photon flux of the solar irradiation (photons/(m^{2}s)), and q is the elementary charge (C).

Fundamental electronic properties were also assessed by impedance spectroscopy. The V_{fb} is the potential at which the space charge region vanishes (W_{SC}=0, see Figure 1.1b). In order to actually measure the V_{fb}, the most powerful technique is impedance spectroscopy (IS), or more specifically, Mott-Schottky analysis[39]. Using this technique the capacitance of the space charge layer, C_{SC}, is measured, and C_{SC}^{-2} is plotted against the applied potential, through the eq. 2.3:

$$C_{SC}^{-2} = \frac{2}{q\varepsilon N_D}\left(V + V_{fb} - \frac{k_B T}{q}\right) \quad (2.3)$$

were q is the elemental charge, ε is the dielectric constant, N_D is the donor density, V is the applied potential and $k_B T$ the Boltzmann constant times the temperature. From this plot, a linear slope can be made through the measured C_{SC}^{-2}, and where the linear regression crosses the x-axis is the V_{fb}. From the slope, N_D can be also determined.

For impedance spectroscopy (IS), a 10 mV amplitude sinusoidal perturbation at frequencies between 0.01 Hz and 1 MHz was used.

Mott–Schottky analysis was performed in the dark at different frequencies (10 Hz, 50 Hz and 100 Hz), from the spectral intervals where C_{SC} remained constant at an applied potential.

Chapter 3: Results and discussion

In this chapter the results of structural and optical characterization of the oxide thin films obtained are described. These results allowed verifying the incorporation of extrinsic dopants into the structure. Also, the results of electrical and photoelectrochemical characterization of the prepared material are presented, in order to correlate these results with their optical properties and evaluate its eventual use as photoanode in a PEC solar cell.

3.1 Structural and optical proprieties of Cr:$Cu_3V_2O_8$ and $Cu_3V_2O_8$ films

In order to optimize both the homogeneity and reproducibility for the preparation of the oxide films, the deposition of the precursor solution was rigorously controlled. In first place, the synthesis of the precursor by a precipitation reaction provided a very easy and versatile way to control both the doping density and the concentration of nanoparticles in the precursor solution. On the other hand, spin coating proved to be the most reproducible method to obtain different film thicknesses by controlling the number of deposited layers of the same volume and concentration.

As shown in Figure 3.1, film thicknesses of 400 nm, 600 nm and 800 nm were obtained for two, three and four deposited layers of the precursor, respectively (spin coating cycles). Deposition of more than four layers of precursor results in inhomogeneous films. Digital pictures of the final obtained oxide films are also shown. The orange color correlates well with the expected one, taking into account the E_g value reported for this material.

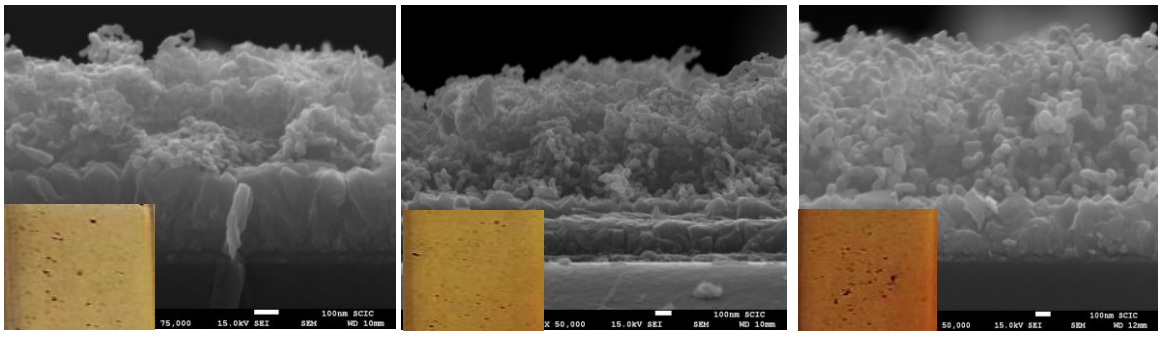

400 nm **600 nm** **800 nm**

Figure 3.1 Cross-sectional SEM images of resulting $Cu_3V_2O_8$ thin films after 425 ºC annealing with different thickness as result of the numbers of deposited layers during the spin coating. Scale bar represents 100 nm in all micrographs.

The morphology and particle size were also determined by SEM (Figure 3.2). The film of the precursor was composed of nanoflakes with around 70-80 nm size, as shown in Figure 3.2a. In contrast, after annealing, both undoped and Cr-doped nanoparticles

showed a globular morphology (Figure 3.2b and c), with lower particle size for the doped nanoparticles (approximately 40-100 nm vs 20-80 nm, respectively).

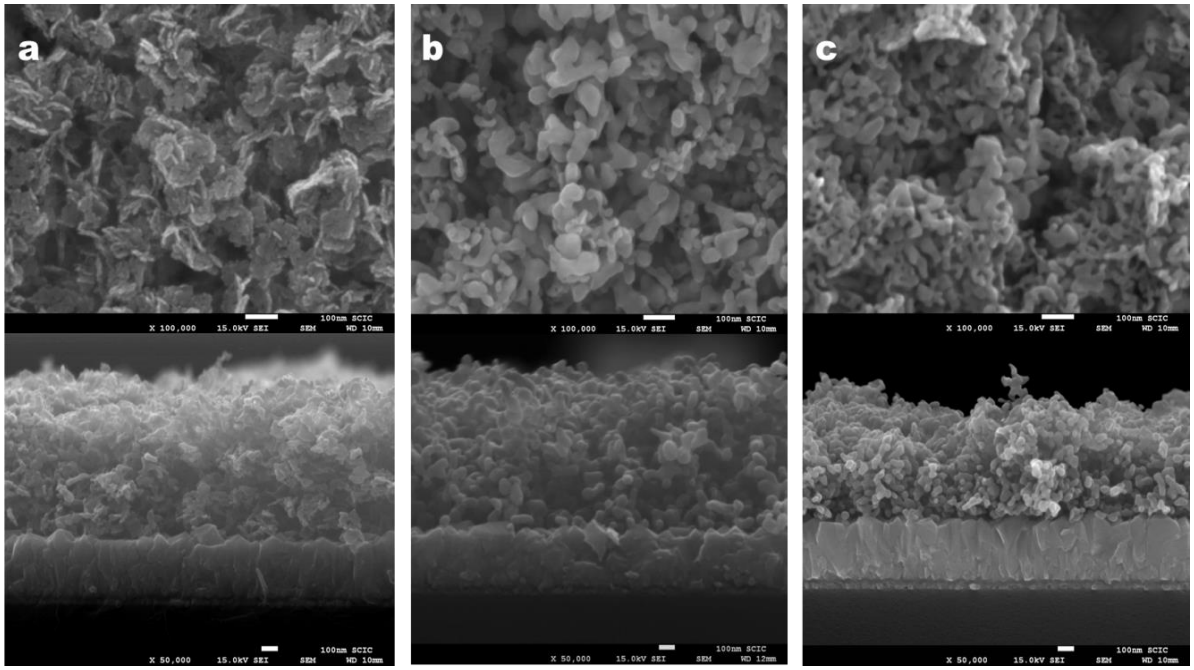

Figure 3.2 Top-views and cross-sectional images obtained by SEM of $Cu_3V_2O_7(OH)_2{\cdot}2H_2O$ (***a***), $Cu_3V_2O_8$ (***b***), and Cr:$Cu_3V_2O_8$ (***c***). Film thickness: 800 nm. Scale bar represents 100 nm in all micrographs.

The crystalline structure of the $Cu_3V_2O_7(OH)_2{\cdot}2H_2O$ precursor was confirmed by XRD analysis, (Figure 3.3). The crystalline system is monoclinic with space group *C*2/*m* and no collateral phases were observed. The structure of the final oxides was also confirmed as a monoclinic system of space group *P*21/*c* in good agreement with the reference pattern. The effect of the incorporation of Cr on the crystalline structure was also studied, finding no representative changes in the patters as to the presence of new phases or notable intensity ratio changes. However, a slight shift of the position (2θ) of the maximum mainly in the [012] crystallographic direction can be noted (inset graph in Figure 3.3) with the increase of Cr content. These shifts are directly related with the interplanar distance through the Bragg´s equation $2d_{hkl}\text{sen}\theta_{hkl} = n\lambda$, showing a clear evidence of the incorporation of Cr in those directions.

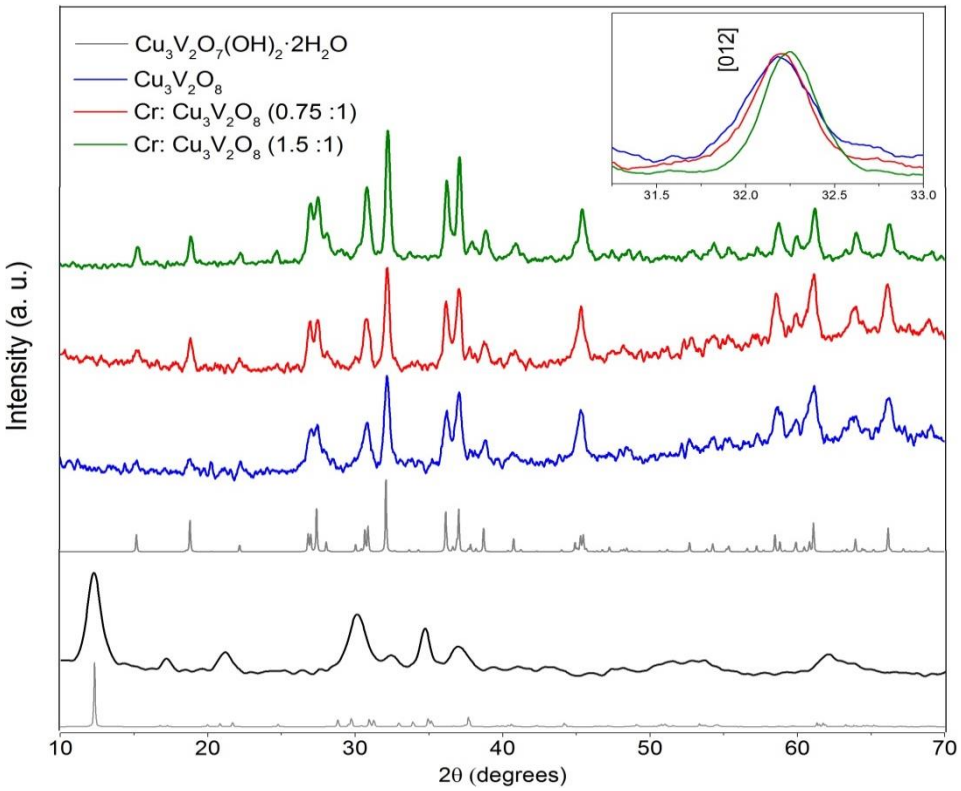

Figure 3.3 XRD spectra of $Cu_3V_2O_7(OH)_2{\cdot}2H_2O$, $Cu_3V_2O_8$ and Cr:$Cu_3V_2O_8$ powders. The reference patterns for these phases are also included: ICSD 68994 for $Cu_3V_2O_7(OH)_2{\cdot}2H_2O$ precursor and ICSD 273110 for $Cu_3V_2O_8$.

The optical properties of the $Cu_3V_2O_8$ films with different thickness values are summarized in Figure 3.4. The absorbance increases monotonically with film thickness as expected, and the films can absorb light up to approximately 600 nm. Figure 3.4 also shows the effect of Cr doping on the optical properties, clearly indicating that the optical response of the $Cu_3V_2O_8$ films are not significantly modified after doping. Since thickness values higher than 800 nm, leads to inhomogeneous films, it was considered 800 nm as the optimum thickness for characterization for the material, although higher absorbance values were obtained for 1000 nm and 1200 nm (Figure 3.4). Actually, the fact that the absorbance is increased for wavelengths higher than 600 nm in the thicker films can be related with increasing of scattering due to the greater irregularity of those films.

In Figure 3.5, the absorbance spectra of 800 nm films are represented and the inset graph shows the Tauc plot for indirect transitions. The calculated indirect bandgap for both undoped and doped $Cu_3V_2O_8$ films (2.0 eV) is in excellent agreement with that previously reported.[30]

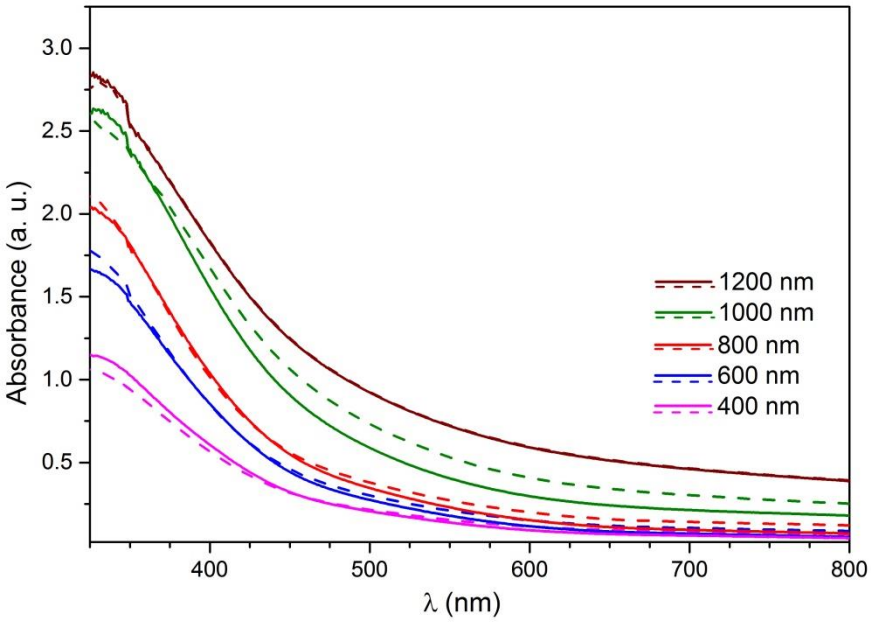

Figure 3.4 Absorbance of $Cu_3V_2O_8$ (dashed lines) and Cr:$Cu_3V_2O_8$ (0.75 at. %) (solid lines) thin films with different thickness values.

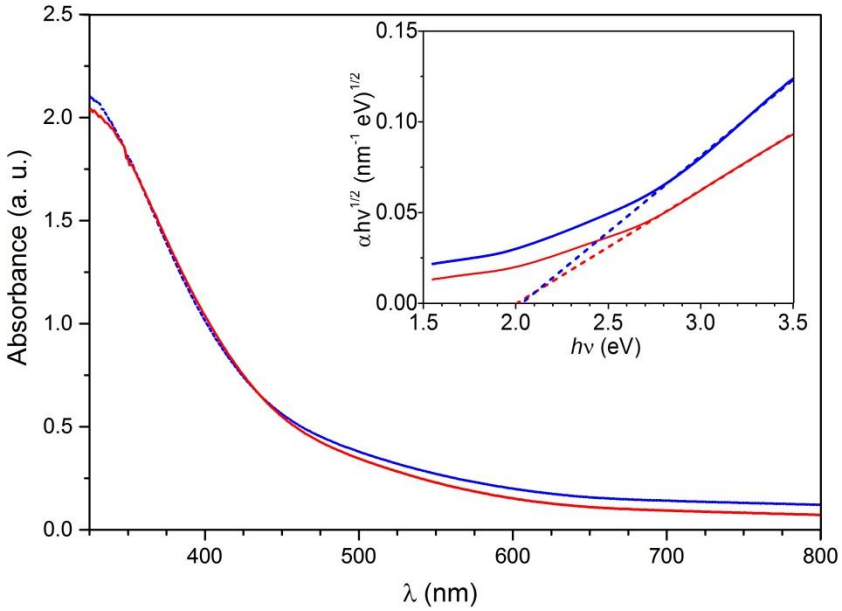

Figure 3.5 Absorbance spectra of $Cu_3V_2O_8$ (blue) and Cr:$Cu_3V_2O_8$ (0.75 at. %) (red) films of 800 nm thickness. Inset: Tauc plots for the determination of the indirect bandgap transition (2.0 eV).

3.2 Effect of dopant and thickness on the photoelectrochemical behavior and the electrical properties.

As mentioned above, in a first attempt to the optimization in the preparation of the electrode, the two parameters, thickness of the film and dopant concentration, were rigorously controlled and its effect on the photoelectrochemical performance of this material as photoanode in a PEC solar cell was studied.

First of all, in order to evaluate the functional performance on the synthesized films as oxygen evolving photoanodes, the *j*-V curves of different thickness $Cu_3V_2O_8$ films were obtained in the dark and under illumination at 100 $mW \cdot cm^{-2}$ in a borate buffer solution (pH 9.2), as depicted in Figure 3.6. Figures 3.6a,b show that the 800 nm thick samples yield the best performance, which can be attributed to the best compromise between homogeneous material distribution and optical absorption. As it was set before, film thicknesses higher than 800 nm led in inhomogeneous material distribution. With respect to the Cr content, in 800 nm films the optimum doping concentration appears at 0.75 at. %, which means a three-fold enhancement at 1.54 V vs RHE compared to pristine $Cu_3V_2O_8$ (Figures 3.6c,d). Higher concentrations of the Cr precursor did not improve the obtained photocurrents.

These results prove that doping can also have a negative influence on the overall performance of the photoelectrode. It can be attributed to the fact that an increasing dopant concentration will decrease the width of *W*, thus narrowing the region of the material in which the internal electric field ensures efficient charge separation. It is therefore essential to maintain the balance between the favorable and unfavorable implications of doping. This is also one of the reasons why in this study it seems to be an optimum dopant concentration at which the photoelectrochemical performance peaks at 0.75 at. % of Cr content (Figure 3.6d).

Figures 3.7a,b show the *j*-V curves for the optimum Cr concentration and film thickness in borate buffer at pH 9.2 in the dark and under front illumination with and without a hole scavenger (0.1 M Na_2SO_3) added to the solution, respectively. The obtained photocurrent density is increased from 66 to 100 $\mu A \cdot cm^{-2}$ at 1.0 V vs RHE due to the Cr-doping. The enhancement reported again for the Cr:$Cu_3V_2O_8$ film indicates that, as a result of the doping process, there is not a significant enhancement of the surface catalytic properties of the photoanode, as is also illustrated by the similar charge injection yield obtained for both undoped and Cr-doped materials, that will be discussed later (Section 3.3, Figure 3.14b).

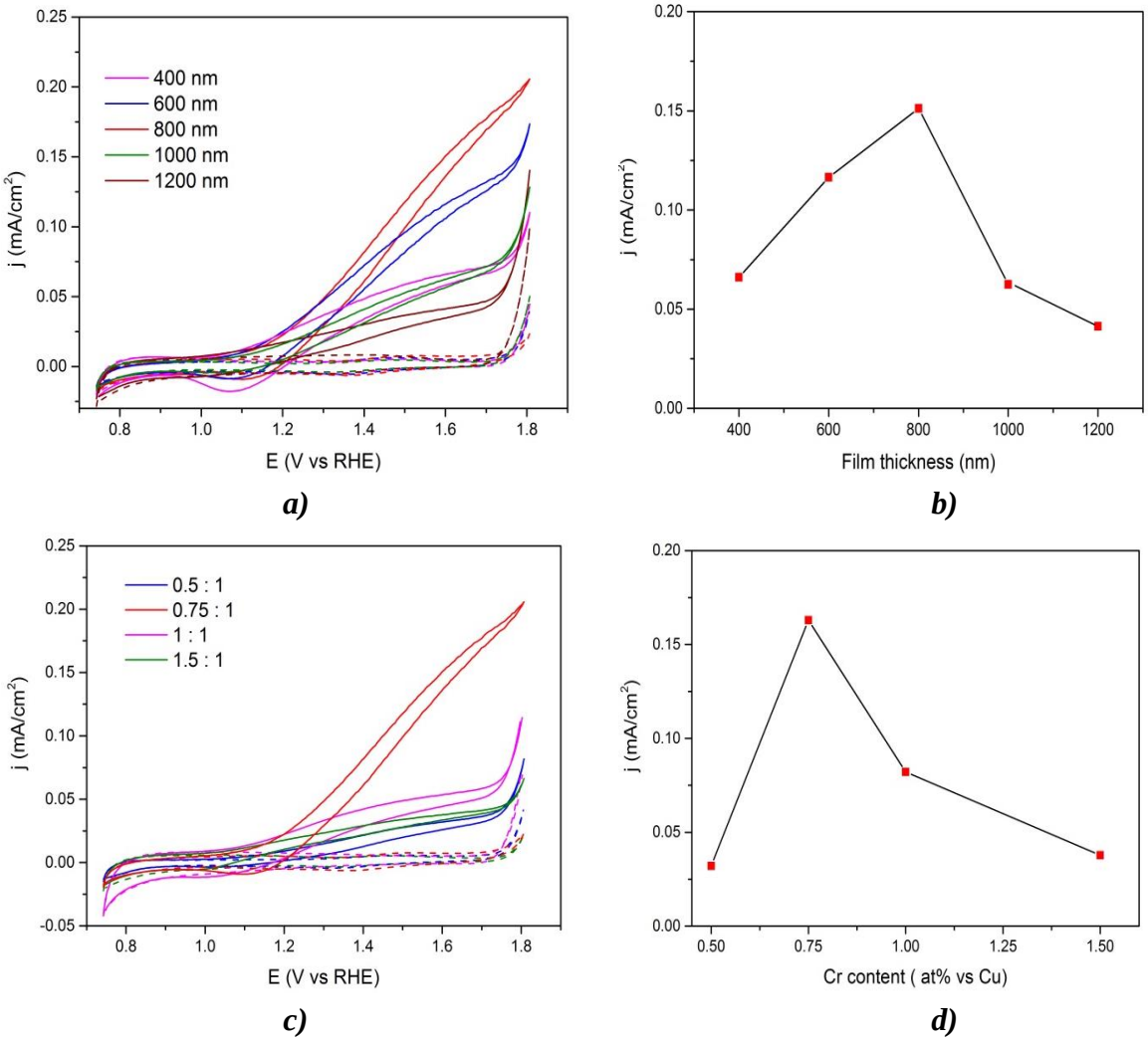

Figure 3.6 *j*-V curves of undoped and Cr-doped $Cu_3V_2O_8$ films in borate buffer at pH 9.2 in the dark (dashed lines) and under front-side illumination at 100 $mW \cdot cm^{-2}$ (dashed lines). ***a)*** Effect of thickness (0.75 at. % Cr content). ***b)*** Photocurrent density at 1.54 V for different film thickness ***c)*** Effect of Cr loading (800 nm thickness). ***d)*** Photocurrent density at 1.54 V for different Cr concentration.

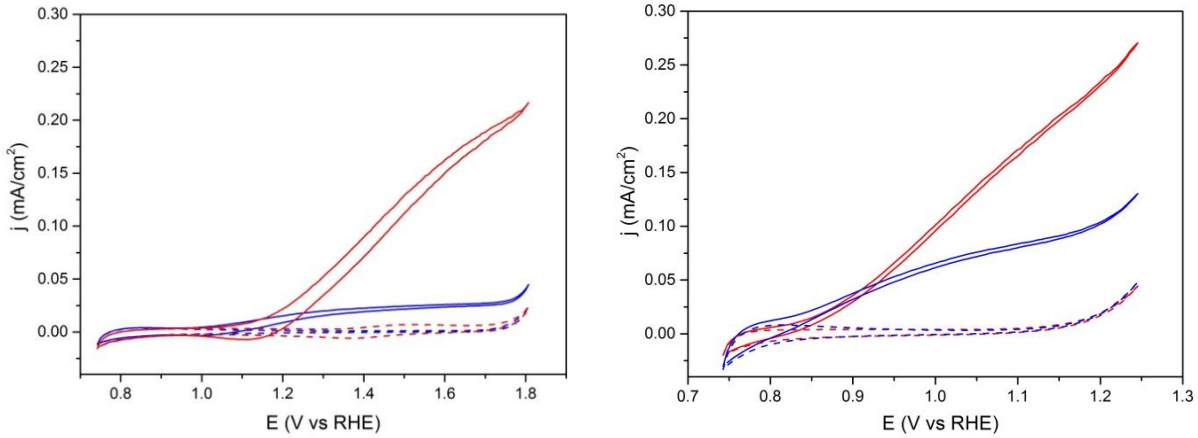

a) ***b)***

Figure 3.7 *j*-V curves of 800 nm $Cu_3V_2O_8$ (blue lines) and Cr:$Cu_3V_2O_8$ (red lines) (0.75 at. %) films obtained in the dark (dashed lines) and under front-side illumination at 100 mW·cm^{-2} (solid lines) in borate buffer at pH 9.2 ***a)*** without and ***b)*** with hole scavenger (0.1 M Na_2SO_3).

The spectral signature of the photocurrent was characterized by IPCE for both the undoped and Cr-doped films without and with the addition of the hole scavenger (Figure 3.8). The insets of this figure display the magnification of the onset region, showing a good correspondence between the onset wavelength in the IPCE and in the absorbance spectra of the films (Figures 3.4 and 3.5), around 600 nm.

The IPCE measures the efficiency of converting an individual photon to an extractable electron and also can be used to estimate the maximum obtainable photocurrent under AM1.5 irradiation. A correlation between IPCE (integrated photocurrent) and information provided by *j–V* measurements is essential for ensuring consistency of measurements.

As illustrated in Table 3.1, there is also an excellent agreement between the integrated photocurrent extracted from the IPCE spectra and that obtained from the *j*-V measurements (Figure 3.7).

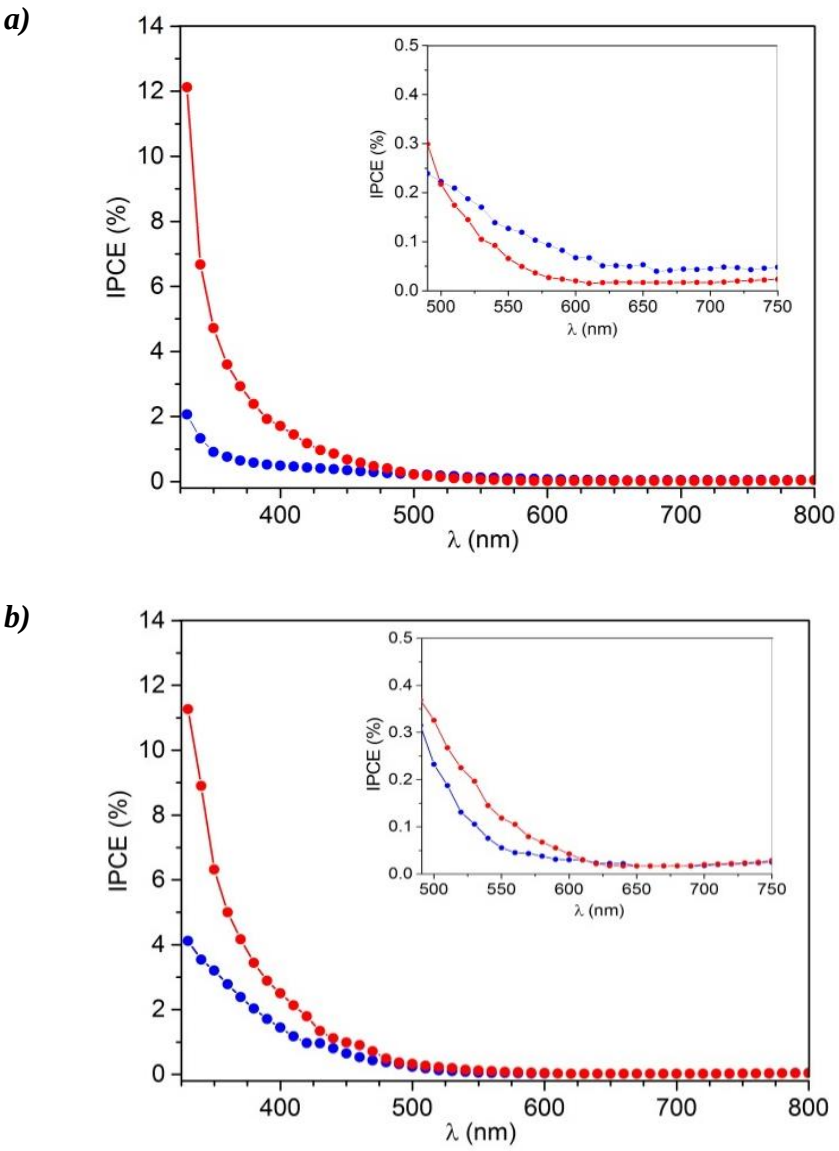

Figure 3.8 IPCE spectra of 800 nm undoped $Cu_3V_2O_8$ (blue symbols) and Cr:$Cu_3V_2O_8$ (red symbols) films obtained in borate buffer at pH 9.2 ***a)*** at 1.54 V vs RHE without hole scavenger and ***b)*** at 1.0 V vs RHE with hole scavenger (0.1 M Na_2SO_3). The inset plots show a magnification of the onset region.

Table 3.1 Integrated currents from IPCE records compared with those obtained from the *j*-V curves. (Reported values were obtained at 1.54 V vs RHE and at 1 V vs RHE for water oxidation and hole scavenger oxidation, respectively).

	Integrated Current ($\mu A/cm^2$)	**Experimental Current ($\mu A/cm^2$)**
$Cu_3V_2O_8$	24	25
$Cu_3V_2O_8$ (in 0.1 M $Na_2SO_{3)}$	52	67
Cr:$Cu_3V_2O_8$	114	113
Cr:$Cu_3V_2O_8$ (in 0.1 M Na_2SO_3)	123	102

In order to evaluate the stability of these films, chronoamperometric measurements were performed at 1.23 V vs RHE for 1h. Figure 3.9 shows the ratio between the potentiostatic photocurrent density *j* and the initial current density j_0 (at t=0), finding a very stable behavior of photocurrent response, with an overall loss of around the 15 % after one hour. This highlights the promising stability of all-first-row transition metal photoanodes.

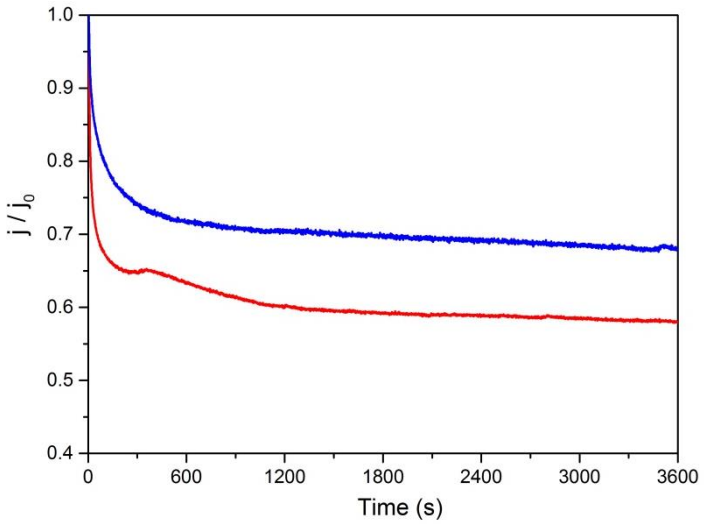

Figure 3.9 Normalized potentiostatic photocurrent density of $Cu_3V_2O_8$ (blue) and Cr:$Cu_3V_2O_8$ (red) films at 1.23 V vs RHE in borate buffer at pH 9.2.

Impedance spectroscopy (IS) measurements were carried out to assess the electronic properties of the $Cu_3V_2O_8$ photoanodes, i.e., N_D and V_{fb}, by means of Mott-Schottky

(MS) plots. The MS plots were obtained directly from the FRA software, through the relation:

$$C_p^{-2} = \left(\frac{(-Z^{"2}+(Z^{'}-R_S)^2)\omega}{-Z^{"}}\right)^2 \quad (3.1)$$

where R_s is the series resistance and was estimated from the high frequency region in the Nyquist plot (Figure 3.10a) and ω is the angular frequency ($2\pi f$). From eq. 2.3 the V_{fb} and N_D were calculated (Table 3.2). The value for the relative dielectric permittivity (ε) was estimated as 44.[40]

This study was performed in the dark covering a wide potential window (from 0 to 1.54 V vs RHE) and at a single frequency, selected from preliminary multi-frequency tests (1 MHz - 100 mHz). The single frequencies were determined from the spectral intervals where C_{SC} remained constant at an applied bias in Bode diagram (Figure 3.10b).

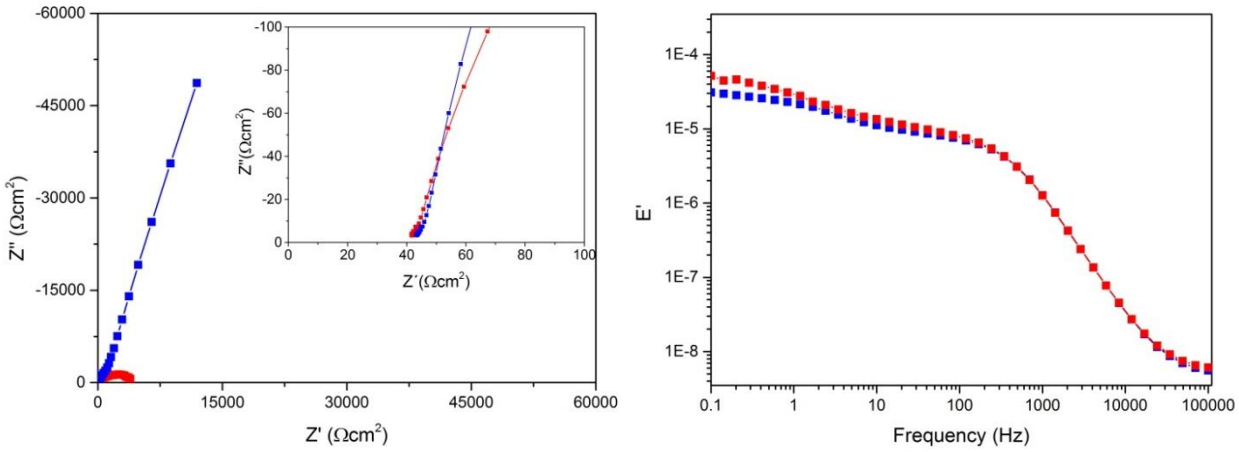

a) ***b)***

Figure 3.10 Representative ***a)*** Nyquist plot and ***b)*** Bode diagram of the impedance spectra obtained on the tested samples in borate buffer at pH 9.2 and dark conditions, at 1.54 V vs RHE. The insets plot in ***a)*** shows a magnification of the high frequency region.

Figure 3.11 compares the MS plots obtained at the frequencies of 10 Hz, 50 Hz and 100 Hz for bare $Cu_3V_2O_8$ films. Note that the MS plots do not change with the applied frequency.

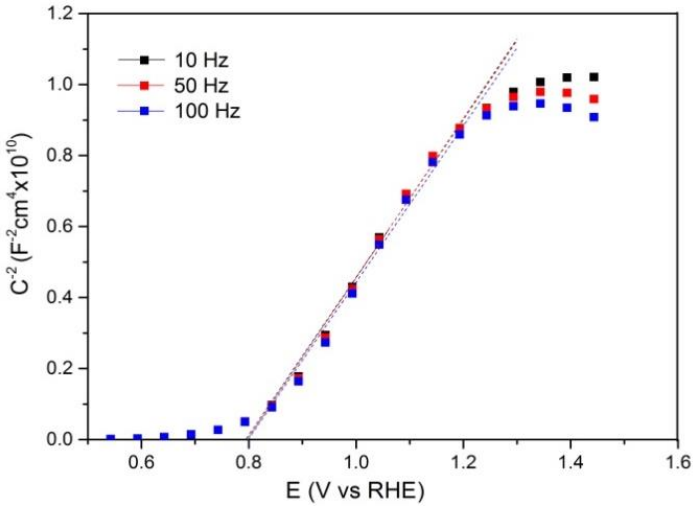

Figure 3.11 Mott-Schottky (MS) plots of $Cu_3V_2O_8$ films performed at 10 Hz, 50 Hz and 100 Hz in borate buffer at pH 9.2, and the linear fitting showing the *x*-intercept corresponding to V_{fb}.

Figure 3.12 shows the MS plots of Cr:$Cu_3V_2O_8$ films with different dopant percent and for a better comparison, in Figure 3.13 the MS plots performed at 10 Hz of bare $Cu_3V_2O_8$ films and Cr:$Cu_3V_2O_8$ films with different dopant concentration are shown. The lower slope reported for the Cr:$Cu_3V_2O_8$ sample is connected to an slight increase in the doping density ($2.21 \cdot 10^{20}$ cm^{-3} vs $1.44 \cdot 10^{20}$ cm^{-3}), which can be attributed to the isomorphic replacement of Cu(II) by Cr(III) in the $Cu_3V_2O_8$ lattice, analogous to the V(V) substitution by Mo(VI) reported in other vanadates.[30, 41] The V_{fb} for $Cu_3V_2O_8$ photoanode is 0.79 V vs RHE, which is slightly more positive than the frequency-dependent values previously reported (between 0.63 and 0.69 V vs RHE)[30]. In addition, the V_{fb} for 0.75 at. % Cr-doped film was around 120 mV cathodically shifted (0.67 V vs RHE); although this beneficial shift is not reflected on the onset potential for the photocurrent (see Figure 3.7a) probably due to the excessive bulk recombination losses.

As can be seen in Table 3.2, the increase of the concentration of Cr in the solution does not imply a higher N_D on the films. XRD analysis do not show the presence of new phases, but a more significant shift of the maximum on the [012] direction (Figure 3.3) was registered, which could be related to a degradation of the film integrity as a result of the strain induced by Cr replacing Cu positions into the periodic crystal lattice, involving the progressive decrease of the photocurrent showed in Figure 3.6c,d for the high Cr additions.

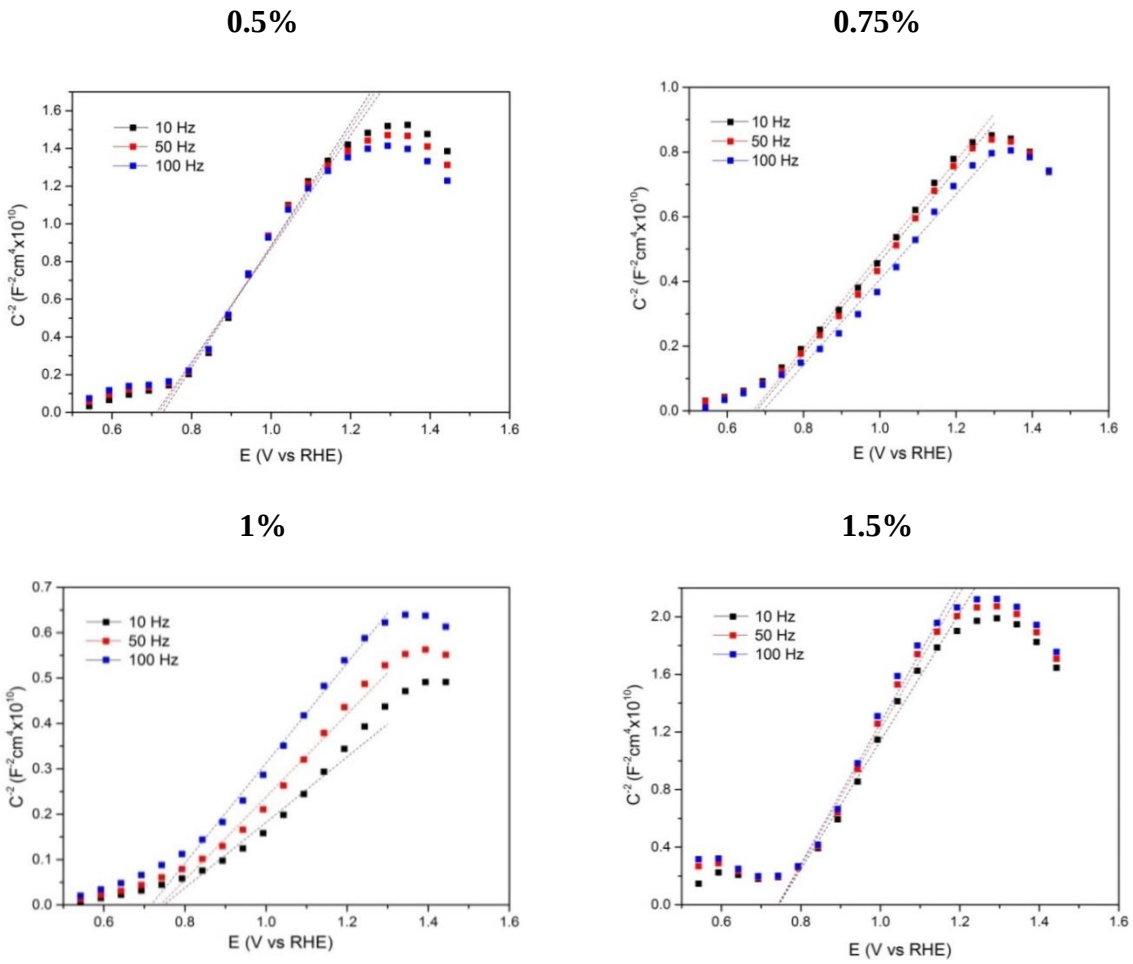

Figure 3.12 Mott-Schottky plot of Cr:$Cu_3V_2O_8$ films with different percent of Cr *vs* Cu content performed at 10 Hz, 50 Hz and 100 Hz in borate buffer at pH 9.2 and the corresponding linear fitting showing the *x*-intercept.

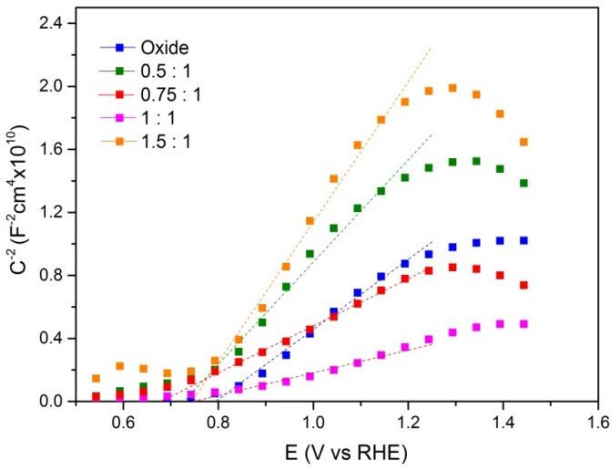

Figure 3.13 Mott-Schottky plot of $Cu_3V_2O_8$ and Cr:$Cu_3V_2O_8$ films performed at 10 Hz in borate buffer at pH 9.2

Table 3.2 Estimated donor density and flat band potential of $Cu_3V_2O_8$ and $Cr:Cu_3V_2O_8$ films from the MS plots at 10 Hz.

	$Cu_3V_2O_8$	$Cr:Cu_3V_2O_8$			
		0.5%	**0.75%**	**1%**	**1.5%**
N_D ($10^{20}cm^{-3}$)	1.44	0.99	2.20	4.44	0.72
V_{fb} (V)	0.79	0.73	0.70	0.75	0.74

3.3 Charge separation and charge injection yields

In order to quantitatively evaluate the limiting factors for performance of the synthesized materials, the charge separation (η_{cs}) and charge injection (η_{cat}) yields were obtained for both doped and un-doped oxide through the relationships showed in eq. 3.2 and 3.3.[42]

$$j_{H_2O} = j_{abs} \times \eta_{cs} \times \eta_{cat} \tag{3.2}$$

$$j_{HS} = j_{abs} \times \eta_{cs} \tag{3.3}$$

Were j_{H2O} and j_{HS} are the obtained photocurrent density in the aqueous electrolyte and in presence of the hole scavenger respectively, and j_{abs} is the maximum photocurrent density obtained if all the electron-hole pairs take part in the OER. From the optical measurements, the j_{abs} was calculated by integrating the solar photon flux (Φ_λ [photons/(m^2s)]), from the lower limit of the measured solar spectrum to the absorption edge (600 nm) of the oxide, shown in eq. 3.4:

$$j_{abs} = \int (\Phi_\lambda \times q) d\lambda \tag{3.4}$$

The calculated theoretical photocurrent was 12.90 mA·cm^{-2} and 11.21 mA·cm^{-2} for 800 nm thick undoped and Cr doped films, respectively.

The comparative behavior of both calculated yields is showed in Figure 3.14. The low η_{cs} values (< 2%) obtained for the undoped material highlight the excessive bulk recombination losses in this material, which constitutes the main limiting factor for performance. Cr doping significantly increases η_{cs}, (with a five-fold enhancement at 1.23 V vs RHE), although the obtained values are still low for further technological deployment of this material. On the other hand, the effect of Cr doping on η_{cat} is negligible

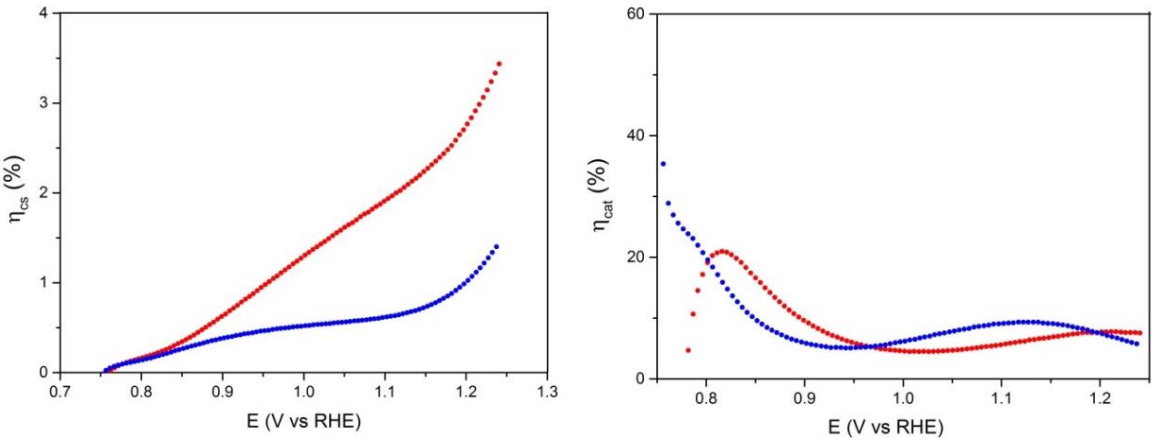

a) ***b)***

Figure 3.14 ***a)*** Charge separation efficiency (η_{cs}) and ***b)*** Charge injection efficiency (η_{cat}) for 800 nm films of $Cu_3V_2O_8$ (blue) and Cr:$Cu_3V_2O_8$ (red)

The addition of water oxidation co-catalysts could significantly enhance this yield, although given the high bulk recombination losses reflected in the low η_{cs} yields, further efforts towards improving the catalytic performance of this material were not attempted.

Conclusions

The optical and photoelectrochemical properties of Cr:$Cu_3V_2O_8$ as a candidate photoanode for photoelectrochemical water splitting were studied and both the effect of thickness and Cr doping aiming at optimizing the performance of the material particularly by overcoming its large bulk recombination losses, were explored.

The determined V_{fb} (0.67 V), E_g (2.0 eV) and E_{VB} (~ 2.5 eV - 2.7 eV), joined to the simple preparation of thin films and good stability, suggest that Cr:$Cu_3V_2O_8$ may be a promising photoanode into a water splitting tandem cell.

The results show that a remarkable improvement of the photocurrent density and the photon-to-current conversion efficiency is obtained after 0.75 at. % Cr doping on 800 nm thin films, which can be related to the increased extrinsic doping of the material. However, further efforts must be carried out in order to achieve competitive charge separation yields (>70%) for technological deployment.

Based on the obtained results, it is propose for future works on this material to overcome first the kinetic barrier at semiconductor surface by introducing a suitable oxygen evolution catalyst. On the other hand, it will be interesting as well the use of function transfer measurements such as Incident Modulated Photocurrent Spectroscopy (IMPS) and/or Incident Modulated Photovoltage Spectroscopy (IMVS) that allow elucidating the mechanisms of charge transport in the bulk material.

References

1. Kamat, P. V., Meeting the Clean Energy Demand: Nanostructure Architectures for Solar Energy Conversion. *The Journal of Physical Chemistry C* **2007**, *111*, 2834-2860.

2. Momirlan, M.; Veziroglu, T. N., The Properties of Hydrogen as Fuel Tomorrow in Sustainable Energy System for a Cleaner Planet. *International Journal of Hydrogen Energy* **2005**, *30*, 795-802.

3. van de Krol, R.; Liang, Y.; Schoonman, J., Solar Hydrogen Production with Nanostructured Metal Oxides. *Journal of Materials Chemistry* **2008**, *18*, 2311-2320.

4. Cho, S.; Jang, J.-W.; Lee, K.-H.; Lee, J. S., Research Update: Strategies for Efficient Photoelectrochemical Water Splitting Using Metal Oxide Photoanodes. *APL Mater.* **2014**, *2*, 010703.

5. Global Hydrogen Fuel Cell Electric Vehicle Market Buoyed as Oems Will Launch 17 Vehicle Models by 2027, Ihs Says. press.ihs.com/press-release/automotive/global-hydrogen-fuel-cell-electric-vehicle-market-buoyed-oems-will-launch-1.

6. Fujishima, A.; Honda, K., Electrochemical Photolysis of Water at a Semiconductor Electrode. *Nature* **1972**, *238*, 37-8.

7. Sivula, K., Metal Oxide Photoelectrodes for Solar Fuel Production, Surface Traps, and Catalysis. *The Journal of Physical Chemistry Letters* **2013**, *4*, 1624-1633.

8. Murphy, A. B.; Barnes, P. R. F.; Randeniya, L. K.; Plumb, I. C.; Grey, I. E.; Horne, M. D.; Glasscock, J. A., Efficiency of Solar Water Splitting Using Semiconductor Electrodes. *International Journal of Hydrogen Energy* **2006**, *31*, 1999-2017.

9. Fujishima, A.; Honda, K., Electrochemical Photolysis of Water at a Semiconductor Electrode. *Nature* **1972**, *238*, 37-38.

10. Nowotny, J.; Bak, T.; Nowotny, M. K.; Sheppard, L. R., Titanium Dioxide for Solar-Hydrogen I. Functional Properties. *International Journal of Hydrogen Energy* **2007**, *32*, 2609-2629.

11. Sivula, K.; Le Formal, F.; Grätzel, M., Solar Water Splitting: Progress Using Hematite (A-Fe2o3) Photoelectrodes. *ChemSusChem* **2011**, *4*, 432-449.

12. Butler, M. A., Photoelectrolysis and Physical Properties of the Semiconducting Electrode Wo2 *Journal of Applied Physics* **1977**, *48*, 1914-1920.

13. Woodhouse, M.; Parkinson, B. A., Combinatorial Approaches for the Identification and Optimization of Oxide Semiconductors for Efficient Solar Photoelectrolysis. *Chemical Society Reviews* **2009**, *38*, 197-210.

14. Abdi, F. F.; Han, L.; Smets, A. H. M.; Zeman, M.; Dam, B.; van de Krol, R., Efficient Solar Water Splitting by Enhanced Charge Separation in a Bismuth Vanadate-Silicon Tandem Photoelectrode. *Nature Communications* **2013**, *4*.

15. Steier, L.; Herraiz-Cardona, I.; Gimenez, S.; Fabregat-Santiago, F.; Bisquert, J.; Tilley, S. D.; Graetzel, M., Understanding the Role of Underlayers and Overlayers in Thin Film Hematite Photoanodes. *Advanced Functional Materials* **2014**, *24*, 7681-7688.

16. Du, C.; Yang, X.; Mayer, M. T.; Hoyt, H.; Xie, J.; McMahon, G.; Bischoping, G.; Wang, D., Hematite-Based Water Splitting with Low Turn-on Voltages. *Angewandte Chemie-International Edition* **2013**, *52*, 12692-12695.

17. Zandi, O.; Hamann, T. W., Enhanced Water Splitting Efficiency through Selective Surface State Removal. *J. Phys. Chem. Lett.* **2014**, *5*, 1522-1526.

18. Kim, T. W.; Choi, K.-S., Nanoporous Bivo4 Photoanodes with Dual-Layer Oxygen Evolution Catalysts for Solar Water Splitting. *Science* **2014**, *343*, 990-994.

19. Suntivich, J.; May, K. J.; Gasteiger, H. A.; Goodenough, J. B.; Shao-Horn, Y., A Perovskite Oxide Optimized for Oxygen Evolution Catalysis from Molecular Orbital Principles. *Science* **2011**, *334*, 1383-1385.

20. Pihosh, Y., et al., Nanostructured Wo3/Bivo4 Photoanodes for Efficient Photoelectrochemical Water Splitting. *Small* **2014**, *10*, 3692-3699.

21. Cesar, I.; Kay, A.; Martinez, J. A. G.; Gratzel, M., Translucent Thin Film Fe2o3 Photoanodes for Efficient Water Splitting by Sunlight: Nanostructure-Directing Effect of Si-Doping. *Journal of the American Chemical Society* **2006**, *128*, 4582-4583.

22. Osterloh, F. E., Inorganic Nanostructures for Photoelectrochemical and Photocatalytic Water Splitting. *Chemical Society Reviews* **2013**, *42*, 2294-2320.

23. Lin, Y.; Zhou, S.; Sheehan, S. W.; Wang, D., Nanonet-Based Hematite Heteronanostructures for Efficient Solar Water Splitting. *Journal of the American Chemical Society* **2011**, *133*, 2398-2401.

24. Bisquert, J.; Cendula, P.; Bertoluzzi, L.; Gimenez, S., Energy Diagram of Semiconductor/Electrolyte Junctions. *The Journal of Physical Chemistry Letters* **2014**, *5*, 205-207.

25. Pihosh, Y., et al., Photocatalytic Generation of Hydrogen by Core-Shell WO_3/$BiVO_4$ Nanorods with Ultimate Water Splitting Efficiency. *Scientific Reports* **2015**, *5*, 11141.

26. Newhouse, P. F.; Boyd, D. A.; Shinde, A.; Guevarra, D.; Zhou, L.; Soedarmadji, E.; Li, G.; Neaton, J. B.; Gregoire, J. M., Solar Fuel Photoanodes Prepared by Inkjet Printing of Copper Vanadates. *Journal of Materials Chemistry A* **2016**, *4*, 7483-7494.

27. Dang, H. X.; Rettie, A. J. E.; Mullins, C. B., Visible-Light-Active NiV_2O_6 Films for Photoelectrochemical Water Oxidation. *The Journal of Physical Chemistry C* **2015**, *119*, 14524-14531.

28. Zhou, L.; Yan, Q.; Shinde, A.; Guevarra, D.; Newhouse, P. F.; Becerra-Stasiewicz, N.; Chatman, S. M.; Haber, J. A.; Neaton, J. B.; Gregoire, J. M., High Throughput Discovery of Solar Fuels Photoanodes in the Cuo-V2o5system. *Adv. Energy Mater.* **2015**, *5*, n/a-n/a.

29. Guo, W.; Chemelewski, W. D.; Mabayoje, O.; Xiao, P.; Zhang, Y.; Mullins, C. B., Synthesis and Characterization of CuV_2O_6 and $Cu_2V_2O_7$: Two Photoanode Candidates for Photoelectrochemical Water Oxidation. *The Journal of Physical Chemistry C* **2015**, *119*, 27220-27227.

30. Seabold, J. A.; Neale, N. R., All First Row Transition Metal Oxide Photoanode for Water Splitting Based on Cu3V2O8. *Chem. Mat.* **2015**, *27*, 1005-1013.

31. Zhang, S.; Sun, Y.; Li, C.; Ci, L., $Cu_3V_2O_8$ Hollow Spheres in Photocatalysis and Primary Lithium Batteries. *Solid State Sciences* **2013**, *25*, 15-21.

32. Dai, J.; Lai, M.; LaFollette, R. M.; Reisner, D., Thin Film Copper Vanadium Oxide Electrodes for Thermal Batteries. *ECS Transactions* **2011**, *33*, 3-9.

33. Jezierski, A.; Kaczkowski, J., Electronic Structure and Thermodynamic Properties of $Cu_3V_2O_8$ Compound. *Phase Transitions* **2015**, *88*, 970-978.

34. Perrot, P., Copper–Oxygen–Vanadium. In *Refractory Metal Systems*, Springer: 2010; pp 240-256.

35. Ghiyasiyan-Arani, M.; Masjedi-Arani, M.; Salavati-Niasari, M., Simple Precipitation Synthesis of Pure $Cu_3V_2O_8$ Nanoparticles and Investigation of Their Optical Properties. *Journal of NanoStructures* **2015**, *5*, 437-441.

36. Zhang, S.; Ci, L.; Liu, H., Synthesis, Characterization, and Electrochemical Properties of $Cu_3V_2O_7$ (Oh) 2· $2H_2O$ Nanostructures. *The Journal of Physical Chemistry C* **2009**, *113*, 8624-8629.

37. Guo, W. L.; Chemelewski, W. D.; Mabayoje, O.; Xiao, P.; Zhang, Y. H.; Mullins, C. B., Synthesis and Characterization of CuV_2O_6 and $Cu_2V_2O_7$: Two Photoanode Candidates for Photoelectrochemical Water Oxidation. *J. Phys. Chem. C* **2015**, *119*, 27220-27227.

38. Hisatomi, T.; Kubota, J.; Domen, K., Recent Advances in Semiconductors for Photocatalytic and Photoelectrochemical Water Splitting. *Chemical Society Reviews* **2014**, *43*, 7520-7535.

39. Klahr, B.; Gimenez, S.; Fabregat-Santiago, F.; Hamann, T.; Bisquert, J., Water Oxidation at Hematite Photoelectrodes: The Role of Surface States. *Journal of the American Chemical Society* **2012**, *134*, 4294-4302.

40. Sarkar, S.; Chattopadhyay, K. K., Size-Dependent Optical and Dielectric Properties of Bivo4 Nanocrystals. *Physica E: Low-dimensional Systems and Nanostructures* **2012**, *44*, 1742-1746.

41. Yin, W.-J.; Wei, S.-H.; Al-Jassim, M. M.; Turner, J.; Yan, Y., Doping Properties of Monoclinic $Bivo_4$ Studied by First-Principles Density-Functional Theory. *Physical Review B* **2011**, *83*, 155102.

42. Dotan, H.; Sivula, K.; Gratzel, M.; Rothschild, A.; Warren, S. C., Probing the Photoelectrochemical Properties of Hematite Alpha-Fe_2O_3) Electrodes Using Hydrogen Peroxide as a Hole Scavenger. *Energy Environ. Sci.* **2011**, *4*, 958-964.